Proceedings of Manufacturing Science and Engineering Conference
MSEC 2020
June 22-26, 2020, Cincinnati, Ohio, USA

MSEC-11256

SKETCH-BASED TENSOR DECOMPOSITION FOR NON-PARAMETRIC MONITORING OF ELECTROSPINNING PROCESSES

Luis Javier Segura
Industrial and Systems Engineering
University at Buffalo, SUNY
Buffalo, New York 14260
Email: lseguras@buffalo.edu

Christian Narváez Muñoz
Departamento de Ciencias de la Energía y Mecánica
Universidad de las Fuerzas Armadas, ESPE
Sangolquí, Ecuador
Email: cpnarvaez1@espe.edu.ec

Chi Zhou
Industrial and Systems Engineering
University at Buffalo, SUNY
Buffalo, New York 14260
Email: chizhou@buffalo.edu

Hongyue Sun
Industrial and Systems Engineering
University at Buffalo, SUNY
Buffalo, New York 14260
Email: hongyues@buffalo.edu

ABSTRACT

Electrospinning is a promising process to fabricate functional parts from macrofibers and nanofibers of bio-compatible materials including collagen, polylactide (PLA), and polyacrylonitrile (PAN). However, the functionality of the produced parts highly rely on quality, repeatability, and uniformity of the electrospun fibers. Due to the variations in material composition, process settings, and ambient conditions, the process suffers from large variations. In particular, the fiber formation in the stable regime (i.e., Taylor cone and jet) and its propagation to the substrate plays the most significant role in the process stability. This work aims to designing a fast process monitoring tool from scratch for monitoring the dynamic electrospinning process based on the Taylor cone and jet videos. Nevertheless, this is challenging since the videos are of high frequency and high dimension, and the monitoring statistics may not have a parametric distribution. To achieve this goal, a framework integrating image analysis, sketch-based tensor decomposition, and non-parametric monitoring, is proposed. In particular, we use Tucker tensor-sketch (Tucker-TS) based tensor decomposition to extract the sparse structure representations of the videos. Additionally, the extracted monitoring variables are non-normally distributed, hence non-parametric bootstrap Hotelling T^2 control chart is deployed to handle this issue during the monitoring. The framework is demonstrated by electrospinning a PAN-based polymeric solution. Finally, it is demonstrated that the proposed framework, which uses Tucker-TS, largely outperformed the computational speed of the alternating least squares (ALS) approach for the Tucker tensor decomposition, i.e., Tucker-ALS, in various anomaly detection tasks while keeping the comparable anomaly detection accuracy.

Keywords: Biocompatible Materials, Electrospinning, Non-parametric Multivariate Control Chart, Tensor Sketch, Video Monitoring

1 Introduction

Continuous structured polymer fibers with diameters ranging from tens of nanometers to several micrometers are of considerable interest for various kinds of applications, such as high performance filters, regenerative medicine, and biomaterial scaffold for cell growth, wound dressings, and tissue engineering [1–4]. Electrospinning has been shown to be a feasible approach that is able to produce such fine fibers, where aqueous solutions of

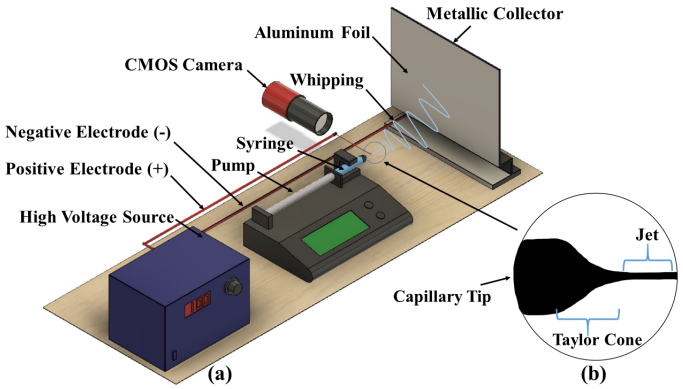

Figure 1. A Scheme of the Electrospinning Process: (a) Electrospinning setup, and (b) Stable regime

biocompatible materials (e.g., collagen, polylactide (PLA), polyacrylonitrile (PAN), etc.) can be electrospun [5].

Figure 1 shows a schematic setup of electrospinning. In particular, a strong electrostatic field is generated between a polymeric aqueous solution contained in a syringe with a capillary tip and a metallic collector. Due to the influence of the electrostatic field, the suspended droplet from the capillary tip is deformed into a conical shape (i.e, Taylor cone). When the voltage surpasses a threshold value, electrostatic force overcome the surface tension of the aqueous solution, thus a fine charged jet is produced, as depicted in Figure 1 (b). The ejected jet travels towards the metallic collector, which acts as a counter electrode. Before the jet lands onto the collector, it thins up under the influence of electrohydrodynamic force [6]. Depending on the operating condition, the charged jet undergoes a series of electrically induced bending instabilities (i.e., whipping, see Figure 1 (a)) that generates considerable stretching [7]. The stretching phenomenon is accompanied by fast evaporation of the solvent and results in substantial reduction in the final diameter of the deposited fibers [8]. Finally, the accumulated fibers on the surface of the collector form a non-woven mat with diameters of the order of nanometers and micrometers.

The uniformity of the fiber diameters is a critical quality-determining factor for functional applications of the nonwoven mats. For instance, the uniformity of diameter controls the porous three-dimensional structure and high-surface volume ratio, which are beneficial for tissue engineering applications [9]. Hence, it is important to guarantee the diameter uniformity in the electrospinning process. The diameter of the fibers can be affected by several parameters, i.e., solution parameters, process parameters, and ambient parameters [4]. For instance, solution parameters, namely viscosity, conductivity, molecular weight, and surface tension, have been extensively studied to improve the processability of aqueous solutions in order to obtain uniform fibers with high mechanical properties in electrospinning [10]. In addition, proper selection of process parameters, such as tip-to-collector distance, voltage, flow rate, among others, has influenced the distribution of the deposited fiber diameters. Several statistical approaches, such as response surface methodology (RSM) and analysis of variance (ANOVA), have been used to optimize the uniformity of the fiber diameters [11, 12]. Ambient parameters, such as temperature and humidity, can also affect the electrospun fibers morphology and diameters [13]. Even though there are several studies that have attempted at understanding and improving the uniformity of electrospun fiber diameters, most of them are performed off-line, and real-time monitoring and control remains a critical challenge.

The stable regime, defined by the Taylor cone and jet as shown in Figure 1 (b), can be modulated by changing the process parameters [14], and the behavior of this regime will reflect the uniformity and diameter of the electrospun fibers. Real-time videos of the Taylor cone and jet can be captured based on which real-time monitoring and control are feasible. For instance, an algorithm of pattern recognition for process control of electrospinning has been developed by tracking the Taylor cone's behaviour in [15]. However, the system performs edge detection of the Taylor cone only for pattern determination, ignoring the jet stability and possible bubbles inside. Additionally, electric current was measured in real-time during the electrospinning process, and the recorded current was associated to the jet behaviours and the morphology of the electrospun mats [16].

The available methods do not fully take advantage of the rich process information that vision systems (e.g., borescope, charged-couple device (CCD) camera, high-speed camera, etc.) may offer. Videos are represented by complex data structure, specifically high-dimensionality and correlation characteristics (i.e., spatio-temporal correlation), and are non-trivial to model [17]. For instance, [17] performed an image-based process monitoring using low-rank tensor decomposition to detect combustion anomalies in the steel tube manufacturing. However, this approach assumes multivariate normal distribution of the monitoring variables and the tensor decomposition is performed by alternative least squares (ALS). ALS can be highly computational expensive, which can affect the efficiency of anomalies detection in fast-changing processes as in electrospinning.

The objective of this paper is to propose a video-based monitoring framework from scratch for the dynamic and non-normal electronspinning monitoring variables. A complementary-metal oxide semiconductor (CMOS) image sensor coupled with an amplifying lens was used to record the videos. The system is able to capture the Taylor cone and jet, as shown in Figure 1 (b). Tucker tensor decomposition via tensor-sketch (TS) and a multivariate non-parametric bootstrap Hotelling (T^2) control chart to monitor the video are integrated. The merit of TS [18] lays on considerably reducing the cost and memory consumption during computation while keeping good accuracy. Thus, the savings can be more evident when the dimensionality of the video

streams grows in a dynamic environment (e.g., continuous ink jet printing (IJP) processes). For instance, videos recorded with high-speed cameras (HSC) at a frequency of several thousands of frames per second. Additionally, for the electrospinning process, it was found that the extracted monitoring variables after using Tucker TS are not normally distributed. Thus, a non-parametric bootstrap approach is used to address this issue.

As will be demonstrated in the Case Study section, this paper designs a monitoring framework from scratch that can accurately detect defects in the electrospinning much faster than the ALS based approach. Although there are several methods dedicated to model high-dimensional data and monitor the extracted variables, to the best of our knowledge, this is the first study dedicated to monitoring the Taylor cone and jet from video streams in the electrospining of biocompatible materials. The proposed framework is compared with the Tucker tensor decomposition via ALS [19]. The results showed that our proposed framework outperformed the computational speed of the ALS method with comparable anomaly detection performance. Such a framework is applicable to other processes with high-dimensional, high-frequency and dynamic measurements, and non-parametric monitoring statistics.

The organization of the paper is as follows. Section 2 will briefly review the related works. The proposed approach will be discussed in Section 3. Section 4 will show the experimental results. Finally, Section 5 will conclude the paper and discuss the future work.

2 Literature Review

2.1 Electrospinning

Electrospinning of bio-materials, such as polyethylene oxide (PEO), PLA, PAN, etc., has shown to be an effective technique to produce macrofibers and nanofibers. Such small fibers can be used to produce functional parts, e.g., scaffolds for cell growth and tissue engineering. However, controlling the uniformity of fiber diameters remains a challenge, which affects the functionality of the produced parts. Empirical and analytical approaches have been used to deal with large diameter variations [20].

Empirical approaches have been most widely explored. On one hand, several studies have been dedicated to tailor solutions to improve the fibers' uniformity. For instance, electrospun mats with fibers of less than 1 μm were obtained in [4] by tayloring polimeric solutions, e.g., Bombyx mori silk with PEO. Zhu et al. [21] analyzed the effects of pH and concentration on electrospinning and rheology of regenerated Bombyx mori silk fibroin aqueous solutions. It was revealed that under certain regimes of pH, the average fiber diameters become smaller and more uniform. Similar studies can be seen in [22, 23]. On the other hand, process and solution parameters have also been studied by empirical statistical methods to improve the uniformity of fibers. Sukigara et al. [11] studied the effect of electrospinning parameters, namely concentration percentage, electric field, and spinning distance, on the morphology and diameter of electrospun Bombyx mori regenerated silk fibroin (RSF) fibers. A factorial design was deployed to investigate the parameters' statistical significance on the fiber diameters, and it was identified that the concentration of the solution was the most significant factor. The reported fiber diameters were $100nm$. In a follow up work, Sukigara et al. [24] realized process optimization and empirical modeling using RSM in the electrospinning of Bombyx mori silk. They were able to produce fiber diameters of $40nm$. See also [25, 26] for similar studies.

Analytical models have also been used to predict and control the uniformity of fiber diameters. An example can be found in [20], where an analytical model for the forces that determine jet diameter during electrospinning as a function of surface tension, flow rate, and electrical current in the jet was presented. The model accuracy was successfully attested by experimentation. In addition, analytical equations linking the electrospun fiber diameter with the process parameters and the characteristics of the polymer solution is shown in [27]. The authors introduced the scaling laws to model the diameter of the jet near to and far from the tip of the needle, and at the collector. After experimentation, the models correspond relatively well with the experimental values.

Although the aforementioned approaches have shown significant progress towards reducing the diameter variability in the electrospinning, they are performed off-line, thus preventing their applicability for real-time monitoring and control.

2.2 Process Monitoring

Currently, due to the development of sensing technologies, process modeling and monitoring have been feasible in emerging technologies, such as additive manufacturing and micro/nano-manufacturing [28]. Specifically, image sensors, such as borescope, CMOS cameras, etc., are able to provide a great amount of information for this purpose. Image sensor information are usually of high frequency and high dimension, and processing this information is challenging. Thus, the widely used dimensional reduction techniques, e.g., principal component analysis (PCA) and unfolded PCA, are utilized to extract features that will be used for later analysis. For instance, Jiang et al. [29] presented liquid crystal display surface uniformity defect inspection using ANOVA and exponentially weighted moving average (EWMA) control chart to detect the size and location of defects. Lin et al. [30] used PCA based on wavelet characteristics for automated surface defect inspection. Lu et al. [31] reported an automatic defect inspection for liquid crystals displays (LCDs) using singular value decomposition. Colosimo et al. [32] developed a spatially weighted PCA for monitoring video image data with application to additive manufacturing. See other related works in [33, 34]. However, these techniques break the

original structure of the data, and this might affect the detection accuracy of defects.

Tensor decomposition has risen as an alternative to the traditional dimensional reduction techniques. Tensor decomposition approaches, such as Tucker and CANDECOMP/PARAFAC (CP), preserve the structure of the original data, and have been recently explored in image-based process monitoring. Yan et al. [17] explored coupled low-rank tensor decomposition with multivariate control charts to develop an image-based monitoring framework. Also, in a subsequent work, Yan et al. [35] presented real-time monitoring of high-dimensional functional data streams via spatio-temporal smooth sparse decomposition. The proposed methods used ALS and proximal methods to solve the formulation of the tensor decomposition. This can be time consuming if continuous updates are necessary in fast-changing processes such as electrospinning. To ameliorate the high computational cost that tensor decomposition may involve, TS [18] is applied for the decomposition in this paper. Additionally, the above mentioned monitoring methods assume multivariate normal distribution of the monitoring variables, which is not necessarily the case in many applications.

Megahed et al. [36] reviewed the image-based monitoring methods, and they pointed out that control chart selection depends on whether the monitoring data follows parametric or non-parametric distributions. Since most of the conventional control charts, e.g., Hotelling T^2, EWMA, assume parametric distributions for their implementation, the non-parametric approaches are not well-explored yet. Phaladiganon et al. [37] presented a bootstrap-based T^2 multivariate control chart approach to deal with non-parametric distributions in the monitoring statistics. Another example can be seen in [38]. In this work, a monitoring framework that couples Tucker-TS tensor decomposition with multivariate bootstrap-based Hotelling T^2 control chart is presented.

3 Approach

3.1 Overview of the Proposed Method

A schematic illustration of the proposed framework is presented in Figure 2. Figure 2 (a) shows the electrospinning setup. Solution, process, and ambient parameters govern the stability of the Taylor cone and jet (i.e., stable regime, see Figure 2 (b)), of the electrospinning process. The stable regime is captured by recording videos with a CMOS camera (Figure 2 (c)). The videos, which are high-dimensional, are used as input data to extract the monitoring statistics, as illustrated in Figure 2 (d). In particular, the videos are pre-processed as shown in Figure 2 (d.1) for later analysis. After that, the in-control image frames are stacked as a tensor T, and Tucker TS tensor decomposition is deployed for feature extraction [17] (see Figure 2 (d.2)). After the tensor decomposition, the tensor factorization matrices and core tensor are extracted. The factorization matrices are used to compute the core tensors G_i for each frame, which serves as the monitoring statistics. The corresponding G_i of each frame is vectorized and the monitoring statistics is obtained for all the in-control samples. Based on these in-control samples, the T^2 statistics can be calculated. It is observed that the vectorized core tensors do not follow multivariate normal distribution. Therefore, a non-parametric method is used to determine the upper control limit (UCL) by bootstrapping the T^2 statistics [37]. Once the factorization matrices and control charts are established based on the in-control frames, the new frames' $G_i s$ are computed and monitored subsequently. The following section is dedicated to explaining the details of the proposed framework.

3.2 Tensor Decomposition and Sketch-based Tensor Decomposition

As mentioned in the Introduction, the electrospinning stable regime, namely Taylor cone and jet, is a critical quality-determining factor towards the consistency and uniformity of the electrospun fiber diameters. Thus, this regime needs to be continuously monitored to assure the quality of the final fibers. Additionally, the stable regime may undergo sudden changes which happen at very high speed. Therefore, high-resolution and high-frequency videos are required to capture these changes. In this way, video data streams grow fast in a short period of time, and this is even more evident if high-speed cameras are used, which usually record videos at very high-resolution and high-frequency, several thousands of pixels and fps, respectively. Due to the abundance of information, extracting interpretable features and common properties from the image frames can be highly computational involving.

In order to address this issue, sparse tensor structures and dimensional reduction techniques (i.e., tensor decomposition) are exploited. Tensor decomposition, a powerful dimensional reduction technique, is used to handle large data representation. The objective of tensor decomposition is to approximate high-dimensional tensors with the tensor product of low dimensional factorization matrices (e.g., U, V, and W) and core tensor (e.g., G) [39], see Figure 3. The framework is illustrated with a third-order tensor $T \in R^{I\times J\times K}$. There are several methods, such as CP and Tucker decomposition methods, that can be used to decompose T [19].

Tucker decomposition is used for this work, as illustrated in Figure 3. T is decomposed by Tucker $T \approx \widetilde{T}^{Tucker} = G \times_1 U \times_2 V \times_3 W = \sum_{l=1}^{L}\sum_{m=1}^{M}\sum_{n=1}^{N} g_{lmn} u_l \circ v_m \circ w_n = [\![G; U, V, W]\!]$, where $U \in \mathbb{R}^{I\times L}$, $V \in \mathbb{R}^{J\times M}$, and $W \in \mathbb{R}^{K\times N}$ are the factorization matrices, and $G \in \mathbb{R}^{L\times M\times N}$ is the core tensor. Consequently, Tucker tensor decomposition is used to extract the monitoring variables for different frames and subsequently determines the T^2 values and UCL. In addition, the factorization matrices and core tensor are used to characterize each frame. The Tucker decomposition

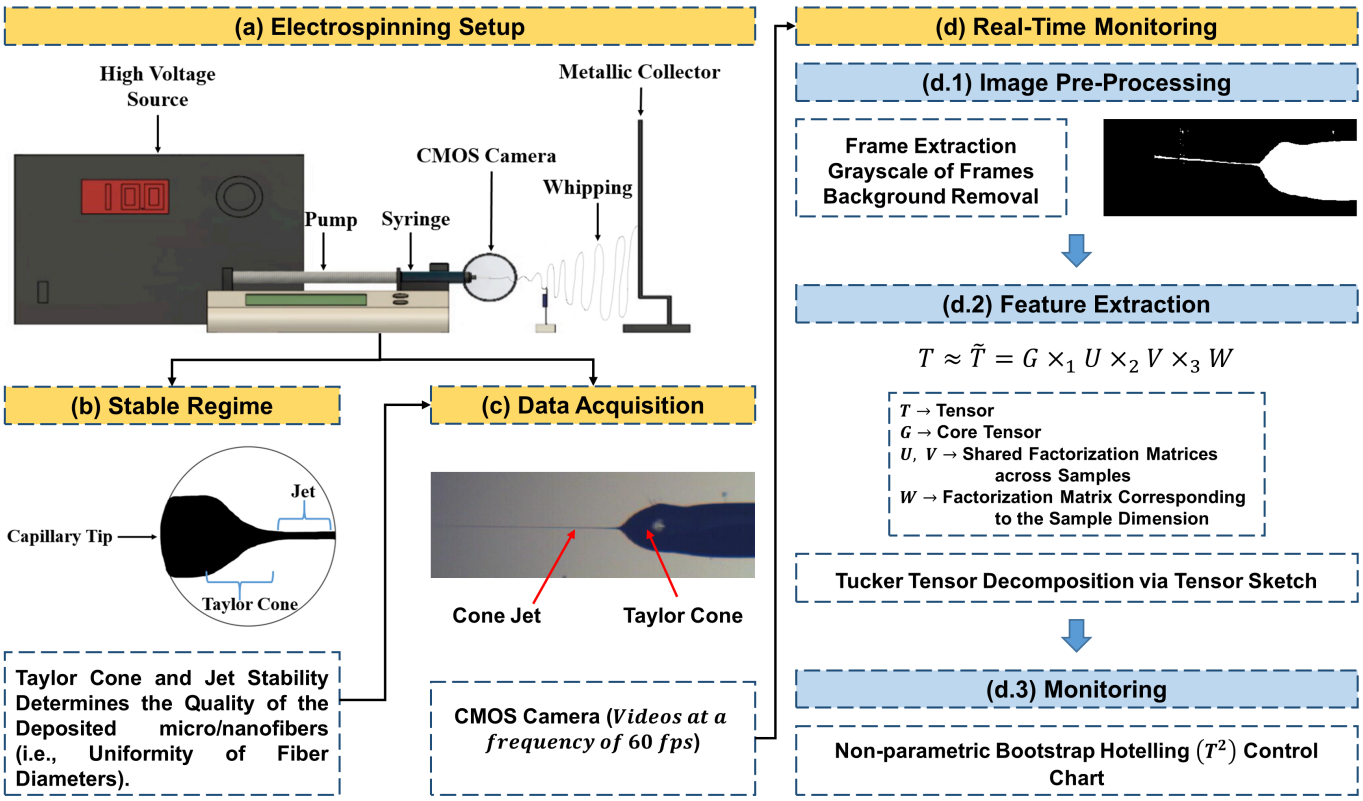

Figure 2. A Schematic Illustration of the Proposed Framework: (a) Electrospinning setup, (b) Stable regime in the Electrospinning, (c) Data acquisition by video recording with a CMOS camera, and (d) Real-time monitoring via Tucker TS and non-parametric T^2 control chart

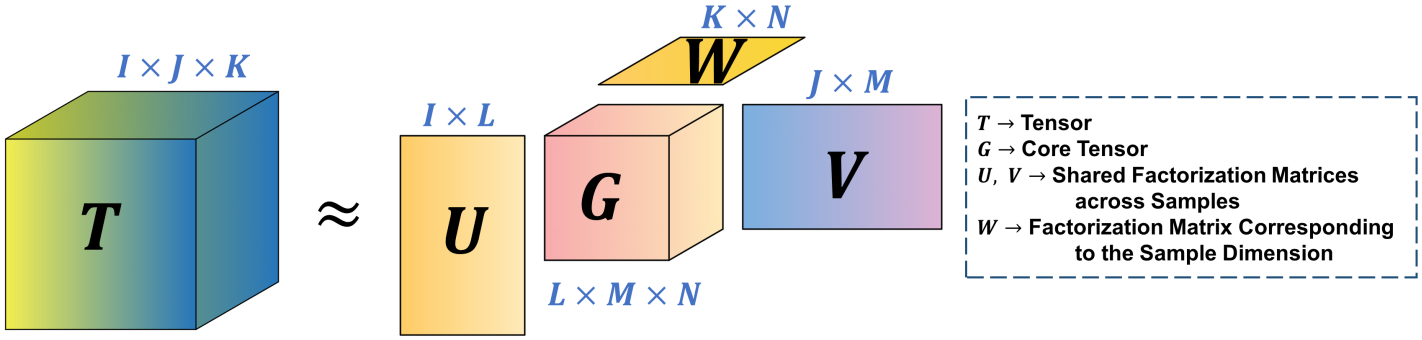

Figure 3. A Schematic Illustration of the Tucker Tensor Decomposition

is formulated as,

$$\underset{G,U,V,W}{\arg\min} \quad \| T - [\![G;U,V,W]\!] \| \tag{1}$$

and can be solved via ALS [18] (i.e. Tucker-ALS). However, Tucker-ALS may suffer from computational issues (e.g., run out-of-memory) as the dimensionality, density (i.e., number of nonzeros), and rank of T increase [18]. An alternative to solving Equation (1) is TS (i.e., Tucker-TS). TS is a technique that performs random projection of the high-dimensional data vectors into lower-dimensional ones. Thus, TS can reduce cost and memory usage of computations at the price of reduced accuracy [18,40]. Particularly, the core tensor and factor matrices are initialized randomly with each element independent and identically distributed (i.i.d.) Uniform (-1,1). Additionally, three operators, i.e., a constant K, the first sketch dimension $J_1 = KR^{Z-1}$, and the second sketch dimension $J_2 = KR^Z$, are defined to ini-

tialize the algorithm, where Z is the size of R and $R_z = R < I$ for all $z \in [Z]$. Values of $K > 1$ work well in practice [18]. The rank $R = [L \quad M \quad N]$ can be determined by structural similarity index (SSIM). SSIM performs a pixel-wise comparison between the tensor T and the approximated tensor $\widetilde{T}^{Tucker}$. The closer SSIM is to 1, the better the approximation is [41]. The rank R needed is usually small compared with the original size of the tensor T. After the tensor decomposition, U and V are shared factorization matrices for $\forall i$, and W is the factorization matrix that corresponds to the sample dimension K for $\forall i$. Tensor multiplication $G_i \times_3 W$ is applied to obtain the individual $g_{i,n}$'s, thus the monitoring variables for $\forall i$ are obtained.

3.3 Control Chart

After the monitoring variables are extracted, one can use Hotelling T^2 multivariate control chart to monitor the electrospinning process. This approach has been extensively used to monitor multivariate processes with individual observations [42]. Assuming that the monitoring variables follow a multivariate normal distribution with mean $\bar{\mathbf{g}}$ and covariance matrix Σ, the T^2 statistics can be calculated by,

$$T^2 = (\mathbf{g} - \bar{\mathbf{g}})^T \Sigma^{-1} (\mathbf{g} - \bar{\mathbf{g}}) \tag{2}$$

where $\mathbf{g}$ is the multivariate mean vector, $\bar{\mathbf{g}}$ is the sample mean vector, and Σ is the covariance matrix of in-control samples. One basic assumption of T^2 control chart is multivariate normality, which is not complied in the electronspinning process monitoring. Thus, a bootstrap-based T^2 multivariate control chart [37] is used to address the non-normality problem. This non-parametric approach does not rely on the assumption of a parametric distribution of the monitoring variables. In order to compute the UCL, the T^2 statistics are first calculated. Then, random bootstrap samples $(i = 1, ..., B)$ from the initial T^2 statistics with replacement are drawn, and it showed that $B > 1000$ is a good estimation [37]. In each of the bootstrapped replications, the $100(1-\alpha)^{th}$ percentile was determined, where $0 < \alpha < 1$. Finally, the average of the B percentile values is set as the UCL [37]. For new samples $\mathbf{g}_{new}$ replaces $\mathbf{g}$ in Equation (2) to compute the new T^2 statistics. Subsequently, they are plotted in the non-parametric Hotelling T^2 control chart for the process monitoring.

4 Case Study

In the electrospinning process, the shape of the Taylor cone and jet are crucial to determine the uniformity of the electrospun fibers. For instance, Figure 4 shows a proper stable regime, i.e., Taylor cone and jet, (Figure 4 (a)), and three improper regimes (Figure 4 (b-d)). It is paramount to detect these instabilities that will derive in fiber diameter defects, thus affecting the functionality of the non-woven mats. The proposed framework is able to detect these faults and will be demonstrated in this section.

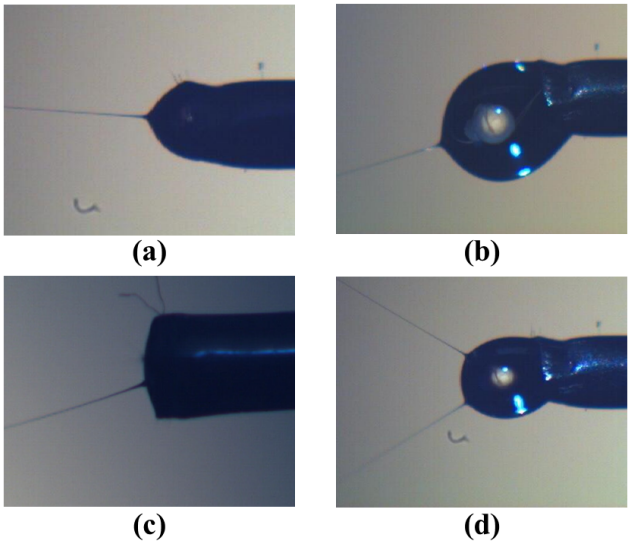

Figure 4. A Comparison of Proper and Improper Regimes: (a) Proper stable regime, (b) Taylor cone with overflow, (c) No Taylor cone formation, and (d) Taylor cone with overflow and double jet

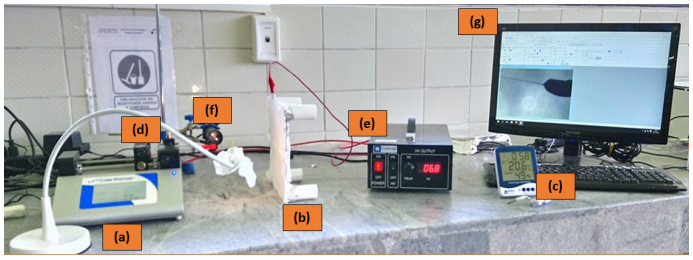

Figure 5. Electrospinning Setup: (a) Syringe pump, (b) Flat collector, (c) Thermo-hygrometer, (d) Syringe, (e) High-voltage source, (f) CMOS camera, and (g) Computer

Figure 5 shows the electrospinning setup that was used for collecting the videos to demonstrate the proposed framework. First, a polymeric solution of PAN at 10% was prepared. The polymeric solution was filled into a syringe container and mounted on a Cole-Parmer syringe pump, see Figure 5 (a) and (d). The pump can supply constant flow at an accuracy of $0.01ml/h$, and a flow rate of $0.4ml/h$ was used. The distance between the tip of the syringe needle and the flat collector is set as $13cm$. The high-voltage source (Figure 5 (e)) supplies voltages of the order of several kV, which in this case was $9kV$. The flat collector (Figure 5(b)) was covered with aluminum foil. Additionally, a CMOS camera (Figure 5 (f)) was used to record the videos that capture part of the tip of the needle, the Taylor cone, and jet (Figure 5 (g)). The resolution of the videos is 480×720 pixels. Finally, a video of 3900 seconds was recorded for this analysis.

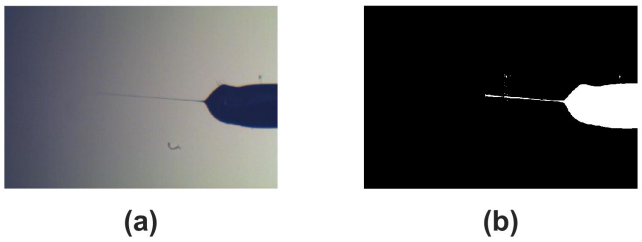

Figure 6. Pre-processed Frame Example: (a) Original frame, and (b) Processed frame

The proposed framework was applied to the recorded video. The recorded video was pre-processed following the procedure shown in Figure 2 (d.1). The unnecessary information was removed so that sparse matrix structures are exploited. A sample of a processed frame can be seen in Figure 6 (b). For this analysis, 1000 in-control frames (i.e., samples) were used for tensor decomposition, feature extraction, and constructing the control chart (determine UCL).

Before applying the tensor decomposition, the 1000 samples were divided into five randomly generated and equally sized folds to determine the rank R via cross-validation (CV). For iterations, four folds were used for training and the remaining fold was used for testing. Thus, the training and testing tensors are of dimensions $T_{Tr} \in \mathbb{R}^{480\times720\times800}$ and $T_{Te} \in \mathbb{R}^{480\times720\times200}$, respectively. In addition, to choose an appropriate rank R for the tensor decomposition, the values of R were incrementally varied, from $[5 \quad 5 \quad 5]$, $[5 \quad 6 \quad 6]$, ..., to $[10 \quad 10 \quad 10]$. For every combination of R, training and testing were repeated for five times. The rank R selection was done by using the SSIM metric (the closer to 1, the better). Table 1 shows the results of the best rank, SSIM index, and corresponding computational time for the Tucker-ALS and Tucker-TS approaches. The rank $R_{ALS} = [8 \quad 5 \quad 5]$ was selected for the construction of the control chart since this is the reference to be compared with, and is expected to have accurate tensor decomposition performance. From Table 1, the proposed Tucker-TS based approach can extract the features for monitoring much faster than the Tucker-ALS approach.

Table 1. Results of best rank, SSIM index, and computational time for Tucker-ALS and Tucker-TS

Approach	Best Rank	SSIM	Time Elapsed (seconds)
Tucker-ALS	[8 5 5]	0.9293	3360.7
Tucker-TS	[9 6 6]	0.9097	1154.8

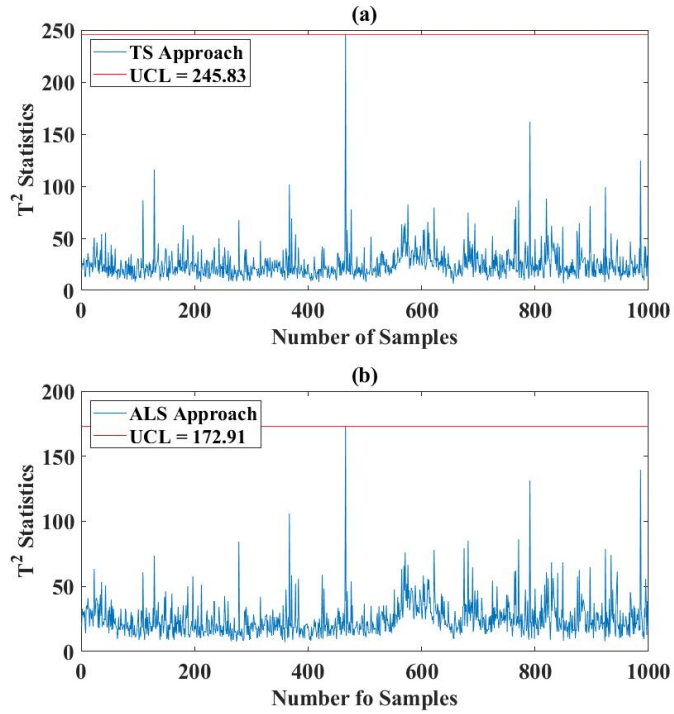

Figure 7. Phase I bootstrap-based Hotelling T^2 control Chart: (a) Control Chart for the Tucker-TS approach, and (b) Control Chart for the Tucker-ALS approach

For the bootstrap Hotelling T^2 control chart, the 1000 pre-processed in-control images are stacked to form a tensor of size $T \in \mathbb{R}^{480\times720\times1000}$. The R_{ALS} was set for the tensor decomposition in both approaches. By using the factorization matrices learned from the tensor decomposition, U and V, the core tensors $g_{i,n}$ for each individual frame were computed and then vectorized. Consequently, the monitoring statistics were extracted. For phase I, the T^2 statistics were calculated by deploying Equation (1) and the UCLs were estimated by choosing the average of 99.95^{th} percentile of the bootstrapped samples. A big percentile (99.95) is used here to accommodate the possible changes in light conditions and background noise, which will affect the pixel density distribution but are not anomalies (As shown in Figure 4, the anomalies are obvious changes in the Taylor cone). 3000 bootstrapping draws were done for this analysis. The in-control non-parametric Hotelling T^2 control charts for the ALS and TS approaches are shown in Figure 7.

In phase II, the UCLs are the same as in phase I. The shared factorization matrices (i.e., U and V), were used to calculate the new core tensors g_{new}. g_{new} was then vectorized to compute the T^2 statistics for the new samples. Subsequently, they were plotted in the T^2 control chart, see Figure 8. In Figure 8, 180 in-control samples and 100 out-of-control samples were included to show the performance of the proposed framework. Figure 8

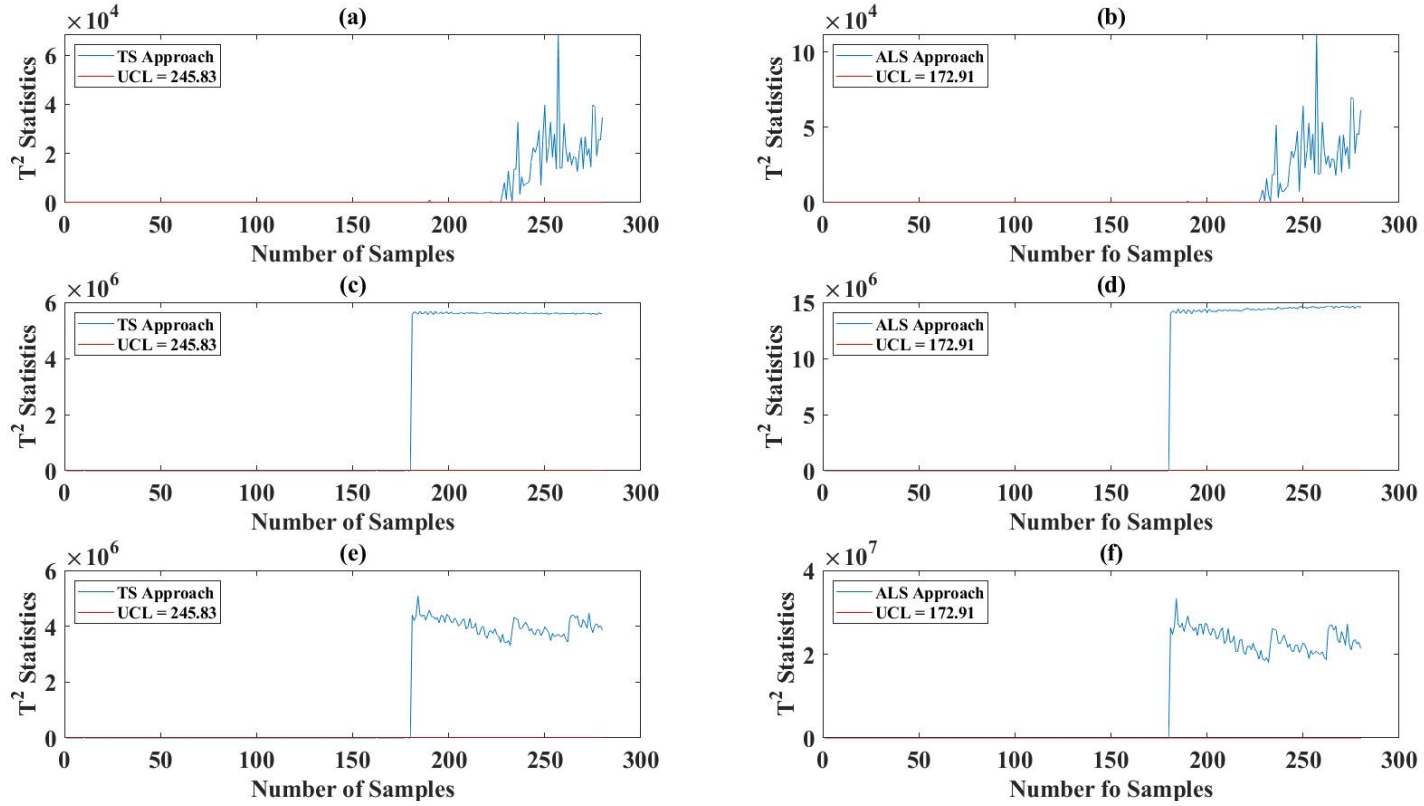

Figure 8. Phase II bootstrap-based Hotelling T^2 control Chart: (a)-(b) Taylor cone with overflow detection, (c)-(d) No Taylor cone formation detection, and (e)-(f) Taylor cone with overflow and double jet detection

shows several fault detection cases (see Figure 4 (b), (c), and (d)) in the electrospinning process. From Figure 8, both approaches can accurately detect sudden changes of the Taylor cone and jet. Note that their false positive rate and false negative rate for the detection are the same, and therefore not shown here.

Moreover, the proposed framework, which uses Tucker-TS for the tensor decomposition, was able to update the shared factorization matrices much faster than the approach that utilized Tucker-ALS while keeping similar accuracy. For instance, for the rank R_{ALS} the Tucker-TS took 5.82 seconds while the Tucker-ALS took 44.65 seconds. Thus, the proposed framework can performed $\approx 87\%$ faster with comparable anomaly detection performance in this study. This is especially beneficial when dynamic updates are necessary, which is the case of electrospinning and many other manufacturing processes, such as IJP.

5 Conclusions

Although electrospinning's potential to produce macrofibers and nanofibers has been widely demonstrated, the process suffers from instabilities that harm the uniformity of the electrospun fibers. These instabilities can be captured by videos, which posses intricate structures (i.e., high-frequency and high-dimensionality), that can be used to monitor the process. Hence, this work presents a framework to address the high-frequency and high-dimensionality of the videos as well as the non-parametric distribution that the monitoring variables may have. Image analysis, sketch-based tensor decomposition, and non-parametric bootstrap based Hotelling T^2 control chart, are integrated in the proposed monitoring framework. The sketch-based approach enables fast feature extraction and control chart establishment for the high-frequency and high-dimensional videos streams over existing methods. It is demonstrated that the sketch-based tensor decomposition (i.e., Tucker-TS approach) largely outperformed the computational speed of the Tucker-ALS approach while keeping the anomaly detection accuracy. Thus, the proposed framework can benefit the fast decision-making in process monitoring and future implementation of closed-loop control. This framework can be applied to other applications with high-frequency and high-dimensional data streams, such as IJP.

In the future, several directions can be investigated. One direction is to explore the non-parametric generalized likelihood ratio (GLR) based approach for change-detection of electrospinning and IJP processes . In GLR, fast computations are required

to continuously update the GLR statistics based on a moving window. Another direction is to explore convolutional neural network (CNN) for anomalies classification of electrospinning and IJP processes. In CNN, the sample size has to be considerably increased. In addition, root-cause identification of the detected anomalies will be investigated, and possible process adjustments will be recommended.

ACKNOWLEDGMENT

L. J. Segura and C. Narváez Muñoz acknowledge the support of the Universidad de las Fuerzas Armadas – ESPE, especially to the rheology and complex fluids laboratory. L. J. Segura, C. Zhou, and H. Sun thank the support from Buffalo SMART and Bluesky.

REFERENCES

[1] Bognitzki, M., Czado, W., Frese, T., Schaper, A., Hellwig, M., Steinhart, M., Greiner, A., and Wendorff, J. H., 2001. "Nanostructured fibers via electrospinning". *Advanced materials,* ***13***(1), pp. 70–72.

[2] Lannutti, J., Reneker, D., Ma, T., Tomasko, D., and Farson, D., 2007. "Electrospinning for tissue engineering scaffolds". *Materials Science and Engineering: C,* ***27***(3), pp. 504–509.

[3] Zhang, X., Reagan, M. R., and Kaplan, D. L., 2009. "Electrospun silk biomaterial scaffolds for regenerative medicine". *Advanced drug delivery reviews,* ***61***(12), pp. 988–1006.

[4] Jin, H.-J., Fridrikh, S. V., Rutledge, G. C., and Kaplan, D. L., 2002. "Electrospinning bombyx mori silk with poly (ethylene oxide)". *Biomacromolecules,* ***3***(6), pp. 1233–1239.

[5] Liao, S., Li, B., Ma, Z., Wei, H., Chan, C., and Ramakrishna, S., 2006. "Biomimetic electrospun nanofibers for tissue regeneration". *Biomedical materials,* ***1***(3), p. R45.

[6] Hohman, M. M., Shin, M., Rutledge, G., and Brenner, M. P., 2001. "Electrospinning and electrically forced jets. ii. applications". *Physics of fluids,* ***13***(8), pp. 2221–2236.

[7] Reneker, D. H., Yarin, A. L., Fong, H., and Koombhongse, S., 2000. "Bending instability of electrically charged liquid jets of polymer solutions in electrospinning". *Journal of Applied physics,* ***87***(9), pp. 4531–4547.

[8] Deitzel, J. M., Kleinmeyer, J., Hirvonen, J., and Tan, N. B., 2001. "Controlled deposition of electrospun poly (ethylene oxide) fibers". *Polymer,* ***42***(19), pp. 8163–8170.

[9] Sisson, K., Zhang, C., Farach-Carson, M. C., Chase, D. B., and Rabolt, J. F., 2010. "Fiber diameters control osteoblastic cell migration and differentiation in electrospun gelatin". *Journal of biomedical materials research Part A,* ***94***(4), pp. 1312–1320.

[10] Thompson, C., Chase, G. G., Yarin, A., and Reneker, D., 2007. "Effects of parameters on nanofiber diameter determined from electrospinning model". *Polymer,* ***48***(23), pp. 6913–6922.

[11] Sukigara, S., Gandhi, M., Ayutsede, J., Micklus, M., and Ko, F., 2003. "Regeneration of bombyx mori silk by electrospinning—part 1: processing parameters and geometric properties". *Polymer,* ***44***(19), pp. 5721–5727.

[12] Kheirkhah Barzoki, P., Latifi, M., and Rezadoust, A. M., 2018. "Response surface methodology optimization of electrospinning process parameters to fabricate aligned polyvinyl butyral nanofibers for interlaminar toughening of phenolic-based composite laminates". *Journal of Industrial Textiles*, p. 1528083718798635.

[13] Li, Z., and Wang, C., 2013. *One-dimensional nanostructures: electrospinning technique and unique nanofibers*. Springer.

[14] Narvaez-Muñoz, C. P., Carrion-Matamoros, L. M., Vizuete, K., Debut, A., Arroyo, C. R., Guerrero, V., Almeida-Naranjo, C. E., Morales-Florez, V., Mowbray, D. J., and Zamora-Ledezma, C., 2019. "Tailoring organic–organic poly (vinylpyrrolidone) microparticles and fibers with multiwalled carbon nanotubes for reinforced composites". *ACS Applied Nano Materials,* ***2***(7), pp. 4302–4312.

[15] Liu, D. L., Jing, C. J., Liu, Y. Y., and Hu, Q. X., 2011. "Algorithm research of pattern recognition for process control of electrospinning". In Advanced Materials Research, Vol. 314, Trans Tech Publ, pp. 1987–1990.

[16] Samatham, R., and Kim, K. J., 2006. "Electric current as a control variable in the electrospinning process". *Polymer Engineering & Science,* ***46***(7), pp. 954–959.

[17] Yan, H., Paynabar, K., and Shi, J., 2014. "Image-based process monitoring using low-rank tensor decomposition". *IEEE Transactions on Automation Science and Engineering,* ***12***(1), pp. 216–227.

[18] Becker, S., and Malik, O. A., 2018. "Low-rank tucker decomposition of large tensors using tensorsketch".

[19] Kolda, T. G., and Bader, B. W., 2009. "Tensor decompositions and applications". *SIAM review,* ***51***(3), pp. 455–500.

[20] Fridrikh, S. V., Jian, H. Y., Brenner, M. P., and Rutledge, G. C., 2003. "Controlling the fiber diameter during electrospinning". *Physical review letters,* ***90***(14), p. 144502.

[21] Zhu, J., Zhang, Y., Shao, H., and Hu, X., 2008. "Electrospinning and rheology of regenerated bombyx mori silk fibroin aqueous solutions: The effects of ph and concentration". *Polymer,* ***49***(12), pp. 2880–2885.

[22] Ayutsede, J., Gandhi, M., Sukigara, S., Ye, H., Hsu, C.-m., Gogotsi, Y., and Ko, F., 2006. "Carbon nanotube reinforced bombyx mori silk nanofibers by the electrospinning process". *Biomacromolecules,* ***7***(1), pp. 208–214.

[23] Pan, H., Zhang, Y., Hang, Y., Shao, H., Hu, X., Xu, Y., and Feng, C., 2012. "Significantly reinforced composite fibers

electrospun from silk fibroin/carbon nanotube aqueous solutions". *Biomacromolecules,* ***13***(9), pp. 2859–2867.

[24] Sukigara, S., Gandhi, M., Ayutsede, J., Micklus, M., and Ko, F., 2004. "Regeneration of bombyx mori silk by electrospinning. part 2. process optimization and empirical modeling using response surface methodology". *Polymer,* ***45***(11), pp. 3701–3708.

[25] Tan, S.-H., Inai, R., Kotaki, M., and Ramakrishna, S., 2005. "Systematic parameter study for ultra-fine fiber fabrication via electrospinning process". *Polymer,* ***46***(16), pp. 6128–6134.

[26] Cui, W., Li, X., Zhou, S., and Weng, J., 2007. "Investigation on process parameters of electrospinning system through orthogonal experimental design". *Journal of applied polymer science,* ***103***(5), pp. 3105–3112.

[27] Cramariuc, B., Cramariuc, R., Scarlet, R., Manea, L. R., Lupu, I. G., and Cramariuc, O., 2013. "Fiber diameter in electrospinning process". *Journal of Electrostatics,* ***71***(3), pp. 189–198.

[28] Colosimo, B. M., 2018. "Modeling and monitoring methods for spatial and image data". *Quality Engineering,* ***30***(1), pp. 94–111.

[29] Jiang*, B., Wang, C.-C., and Liu, H.-C., 2005. "Liquid crystal display surface uniformity defect inspection using analysis of variance and exponentially weighted moving average techniques". *International Journal of Production Research,* ***43***(1), pp. 67–80.

[30] Lin, H.-D., Chung, C.-Y., and Lin, W.-T., 2008. "Principal component analysis based on wavelet characteristics applied to automated surface defect inspection". *WSEAS Transactions on Computer Research,* ***3***(4), pp. 193–202.

[31] Lu, C.-J., and Tsai, D.-M., 2005. "Automatic defect inspection for lcds using singular value decomposition". *The International Journal of Advanced Manufacturing Technology,* ***25***(1-2), pp. 53–61.

[32] Colosimo, B. M., and Grasso, M., 2018. "Spatially weighted pca for monitoring video image data with application to additive manufacturing". *Journal of Quality Technology,* ***50***(4), pp. 391–417.

[33] Megahed, F. M., Wells, L. J., Camelio, J. A., and Woodall, W. H., 2012. "A spatiotemporal method for the monitoring of image data". *Quality and Reliability Engineering International,* ***28***(8), pp. 967–980.

[34] Sun, H., Wang, K., Li, Y., Zhang, C., and Jin, R., 2017. "Quality modeling of printed electronics in aerosol jet printing based on microscopic images". *Journal of Manufacturing Science and Engineering,* ***139***(7), p. 071012.

[35] Yan, H., Paynabar, K., and Shi, J., 2018. "Real-time monitoring of high-dimensional functional data streams via spatio-temporal smooth sparse decomposition". *Technometrics,* ***60***(2), pp. 181–197.

[36] Megahed, F. M., Woodall, W. H., and Camelio, J. A., 2011. "A review and perspective on control charting with image data". *Journal of Quality Technology,* ***43***(2), pp. 83–98.

[37] Phaladiganon, P., Kim, S. B., Chen, V. C., Baek, J.-G., and Park, S.-K., 2011. "Bootstrap-based t 2 multivariate control charts". *Communications in Statistics—Simulation and Computation®,* ***40***(5), pp. 645–662.

[38] Mostajeran, A., Iranpanah, N., and Noorossana, R., 2018. "An explanatory study on the non-parametric multivariate t2 control chart". *Journal of modern applied statistical methods,* ***17***(1), p. 12.

[39] Segura, L. J., Zhao, G., Zhou, C., and Sun, H., 2019. "Nearest-neighbor gaussian process emulation for multidimensional array responses in freeze nano 3d printing of energy devices". *Journal of Computing and Information Science Engineering,* ***Accepted for publication***.

[40] Cao, Y., Thompson, A., Wang, M., and Xie, Y., 2015. "Sketching for sequential change-point detection". *arXiv preprint arXiv:1505.06770*.

[41] Wang, Z., Bovik, A. C., Sheikh, H. R., Simoncelli, E. P., et al., 2004. "Image quality assessment: from error visibility to structural similarity". *IEEE transactions on image processing,* ***13***(4), pp. 600–612.

[42] Hotelling, H., 1947. "Multivariate quality control. techniques of statistical analysis". *McGraw-Hill, New York*.